Direct manipulation of a superconducting spin qubit strongly coupled to a transmon qubit

Pita-Vidal, Marta; Bargerbos, Arno; Splitthoff, Lukas J.; Grünhaupt, Lukas; Wesdorp, Jaap J.; Liu, Yu; Kouwenhoven, Leo P.; van Heck, Bernard; Andersen, Christian Kraglund; More Authors

DOI
10.1038/s41567-023-02071-x

Publication date
2023

Document Version
Final published version

Published in
Nature Physics

Citation (APA)
Pita-Vidal, M., Bargerbos, A., Splitthoff, L. J., Grünhaupt, L., Wesdorp, J. J., Liu, Y., Kouwenhoven, L. P., van Heck, B., Andersen, C. K., & More Authors (2023). Direct manipulation of a superconducting spin qubit strongly coupled to a transmon qubit. *Nature Physics*, (8), 1110-1115. https://doi.org/10.1038/s41567-023-02071-x

nature physics

Article

https://doi.org/10.1038/s41567-023-02071-x

Direct manipulation of a superconducting spin qubit strongly coupled to a transmon qubit

Received: 1 September 2022

Accepted: 26 April 2023

Published online: 22 May 2023

Check for updates

Marta Pita-Vidal[1,9] ✉, Arno Bargerbos[1,9], Rok Žitko[2,3], Lukas J. Splitthoff[1], Lukas Grünhaupt[1], Jaap J. Wesdorp[1], Yu Liu[4], Leo P. Kouwenhoven[1], Ramón Aguado[5], Bernard van Heck[6,7], Angela Kou[8] & Christian Kraglund Andersen[1] ✉

Spin qubits in semiconductors are a promising platform for producing highly scalable quantum computing devices. However, it is difficult to realize multiqubit interactions over extended distances. Superconducting spin qubits provide an alternative by encoding a qubit in the spin degree of freedom of an Andreev level. These Andreev spin qubits have an intrinsic spin–supercurrent coupling that enables the use of recent advances in circuit quantum electrodynamics. The first realization of an Andreev spin qubit encoded the qubit in the excited states of a semiconducting weak link, leading to frequent decay out of the computational subspace. Additionally, rapid qubit manipulation was hindered by the need for indirect Raman transitions. Here we use an electrostatically defined quantum dot Josephson junction with large charging energy, which leads to a spin-split doublet ground state. We tune the qubit frequency over a frequency range of 10 GHz using a magnetic field, which also enables us to investigate the qubit performance using direct spin manipulation. An all-electric microwave drive produces Rabi frequencies exceeding 200 MHz. We embed the Andreev spin qubit in a superconducting transmon qubit, demonstrating strong coherent qubit–qubit coupling. These results are a crucial step towards a hybrid architecture that combines the beneficial aspects of both superconducting and semiconductor qubits.

Spin qubits in semiconductors[1,2] and transmon qubits in superconducting circuits[3] are currently two of the most promising platforms for quantum computing. Spin qubits are promising from a scalability standpoint due to their small footprint and compatibility with industrial semiconductor processing[4]. However, despite encouraging progress in recent years[5–10], spin qubit architectures face challenges in realizing multiqubit interactions over extended distances. Transmon-based circuits currently boast some of the largest numbers of qubits on a

[1]QuTech and Kavli Institute of Nanoscience, Delft University of Technology, Delft, The Netherlands. [2]Jožef Stefan Institute, Ljubljana, Slovenia. [3]Faculty of Mathematics and Physics, University of Ljubljana, Ljubljana, Slovenia. [4]Center for Quantum Devices, Niels Bohr Institute, University of Copenhagen, Copenhagen, Denmark. [5]Instituto de Ciencia de Materiales de Madrid (ICMM), Consejo Superior de Investigaciones Científicas (CSIC), Madrid, Spain. [6]Leiden Institute of Physics, Leiden University, Leiden, The Netherlands. [7]Dipartimento di Fisica, Università di Roma 'La Sapienza', Rome, Italy. [8]Department of Physics and Frederick Seitz Materials Research Laboratory, University of Illinois Urbana-Champaign, Urbana, IL, USA. [9]These authors contributed equally: Marta Pita-Vidal, Arno Bargerbos. ✉e-mail: m.pitavidal@tudelft.nl; c.k.andersen@tudelft.nl

https://doi.org/10.1038/s41567-023-02071-x

single device[11,12], and are readily controlled, read and coupled over long distances due to the use of circuit quantum electrodynamics (QED) techniques[13–15]. However, transmon qubits have a small anharmonicity, limiting the speed of qubit operations, and they are relatively large (typically 0.01 to 1.00 mm^2 per qubit), which leads to large chip sizes and makes transmons susceptible to cross-coupling with distant control elements.

A potential route to leverage the benefits of both superconducting qubits and spin qubits is to encode a qubit in the spin degree of freedom of a quasiparticle occupying an Andreev bound state in a Josephson junction[16,17]. These states are confined by Andreev reflections at the superconducting interfaces and thus are localized in a small and well-defined region, similar to conventional spin qubits. Furthermore, in the presence of spin–orbit interaction (SOI), the supercurrent across the Josephson junction becomes spin dependent[16,18], which allows for interfacing with superconducting circuit elements. Such a superconducting spin qubit has recently been realized in the weak link of a superconductor–semiconductor hybrid nanowire[19], where it was named the Andreev spin qubit (ASQ). This first implementation showed that an ASQ can be efficiently read using standard circuit QED techniques[20]. However, qubit control was hindered by frequent leakage out of the computational subspace of the qubit, formed by higher-energy Andreev levels of the junction. Additionally, due to the selection rules of the system in the absence of a magnetic field[21], direct driving of the ASQ is partly suppressed[22] and qubit manipulation may require the virtual driving of auxiliary states to induce qubit transitions[19].

In this work, we utilize previous insights from semiconducting spin–orbit qubits (SOQ)[23,24] to construct an ASQ using a quantum dot within a Josephson junction[25,26]. To enhance the confinement of the quantum dot, we implement it in a Josephson junction shorter than that used in another work[19] and we use three electrostatic bottom gates. These two features lead to an enhanced charging energy of the dot compared with that in previous implementations of ASQs, such that it can be exploited to deterministically prepare the quantum dot into a doublet phase[25] with well-defined spin-split states. As a consequence, the computational subspace of the qubit is now formed by the lowest-energy states of the junction in the doublet phase. Moreover, this charging energy enhances the parity lifetime of the doublet subspace to the millisecond regime, thereby providing protection against leakage resulting from parity switches of the junction[17] (Supplementary Information). Furthermore, this design allows for fast and direct qubit control through spin–orbit-mediated electric-dipole-induced spin resonance[23,24,27,28]. We additionally demonstrate the magnetic field tunability of the qubit transition frequency over a frequency range of more than 10 GHz, pushing the device into a parameter regime inaccessible to previous experiments, which allows us to investigate the origin of dephasing. At elevated qubit frequencies, this moreover results in a suppression of the population of the excited state, facilitating qubit manipulation and readout without any additional steps needed for the initialization of the qubit beyond qubit relaxation. Finally, the intrinsic coupling between the spin degree of freedom and the supercurrent facilitates strong coherent coupling between the ASQ and a transmon qubit.

ASQ

We implement the ASQ in a quantum dot Josephson junction formed in a hybrid InAs/Al semiconducting–superconducting nanowire (Fig. 1a). The quantum dot is electrostatically defined by three gate electrodes under an uncovered InAs section of the nanowire and tunnel coupled to the superconducting segments[25]. In the limit of weak coupling between the superconducting part of the nanowire and the quantum dot and in the presence of a magnetic field, the ASQ can be described by the effective Hamiltonian[17,26]

$$H_s = E_0 \cos(\phi) - E_{SO}\vec{\sigma}\cdot\vec{n}\,\sin(\phi) + \frac{1}{2}\vec{E}_Z\cdot\vec{\sigma}, \qquad (1)$$

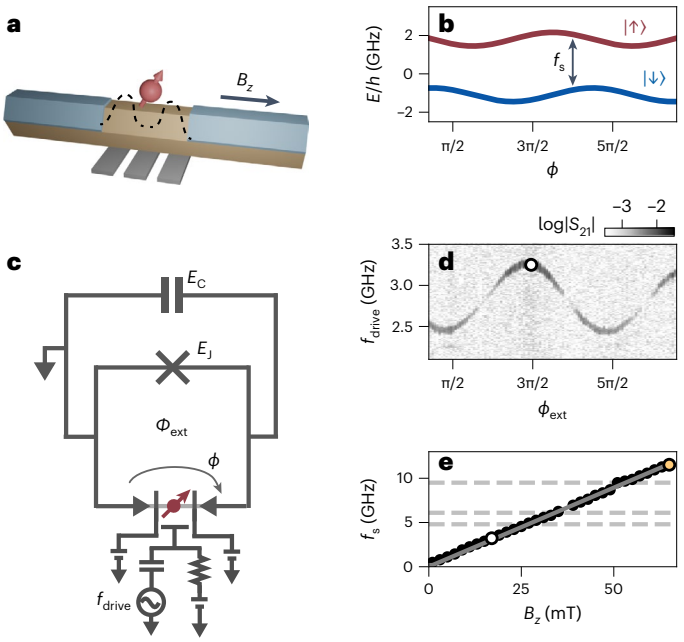

Fig. 1 | ASQ. a, Schematic of an ASQ in a hybrid superconductor–semiconductor nanowire. The qubit is formed in a gate-defined quantum dot with an odd number of electrons and is coupled to superconducting leads. The dashed line is a sketch of the potential landscape created by the gates. **b**, Eigenenergies of the ASQ levels as a function of the phase difference ϕ, as described by the effective model of equation (1). The frequency of the qubit spin-flip transition $|\downarrow\rangle\leftrightarrow|\uparrow\rangle$ is denoted by f_s. Here the component of the Zeeman energy parallel to the zero-field spin-polarization direction is $E_Z^{\parallel} = 2.9$ GHz. **c**, Circuit model of the ASQ embedded in a transmon circuit. The spin state is manipulated by a microwave drive, at frequency f_{drive}, applied to the central gate electrode. The transmon island, with charging energy E_c, is connected to ground by a SQUID formed by the parallel combination of the ASQ and a reference Josephson junction. Here ϕ denotes the superconducting phase difference across the quantum dot junction, whereas Φ_{ext} is the externally applied magnetic flux through the SQUID loop. **d**, Transmission through the readout circuit, S_{21}, as a function of the external flux and applied drive frequency, measured at a magnetic field $B_z = 17$ mT parallel to the nanowire (Supplementary Information). **e**, Extracted qubit frequency f_s versus B_z (markers), measured at $\phi_{ext} = 3\pi/2$. The data are fitted with a linear dependence (solid line), resulting in an effective Landé g-factor of $g^* = 12.7 \pm 0.2$. The horizontal dashed lines denote, from bottom to top, the first transmon frequency, readout resonator frequency and second transmon frequency. The white markers in **d** and **e** indicate the data taken at the same flux and field conditions. The orange marker in **e** indicates the magnetic field used for Figs. 2 and 3.

where ϕ is the phase difference across the junction, $\vec{\sigma}$ is the spin operator, $\vec{n}$ is a unit vector along the zero-field spin-polarization direction (set by the SOI) and $\vec{E}_Z$ is a Zeeman field arising in the presence of an external magnetic field. Here E_0 denotes the effective Josephson energy of the quantum dot junction, common for both spin states. We note that the the term proportional to E_0 has a minimum at $\phi = \pi$, originating from the odd occupancy of the quantum dot junction[26]. In turn, E_{SO} denotes the spin-dependent contribution to the energy of the junction. The spin-dependent potential energy originates from the occurrence of electron co-tunnelling accompanied by a spin flip, and it is finite only if SOI is present and multiple levels of quantum dot are involved in the co-tunnelling sequence[17]. The difference between the energies of the $|\downarrow\rangle$ and $|\uparrow\rangle$ eigenstates of equation (1) determines the ASQ frequency $f_s = E_\uparrow - E_\downarrow$ (Fig. 1b). For readout and control, we embed the ASQ into a superconducting transmon circuit (Fig. 1c). The transmon circuit consists of a capacitor, with charging energy E_c, shunting a

https://doi.org/10.1038/s41567-023-02071-x

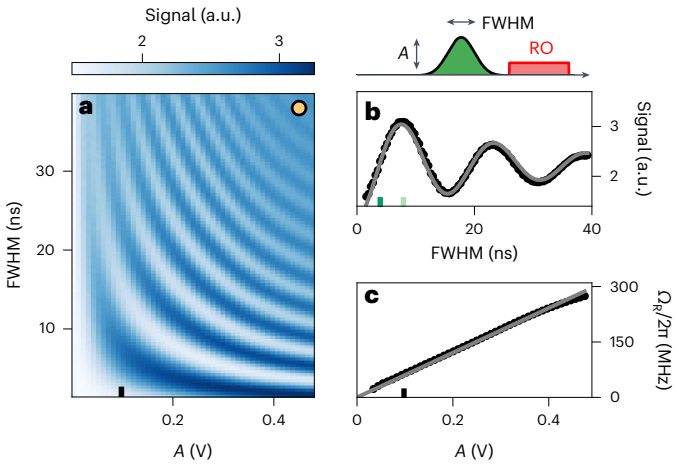

Fig. 2 | Coherent manipulation of the ASQ. Measured at $f_s = 11.5$ GHz at $B_z = 65$ mT. **a**, Rabi oscillations for a range of Gaussian pulses characterized by their amplitude A at the waveform generator output and their FWHM (see the pulse sequence). As also indicated in the pulse sequence, the Rabi pulse is immediately followed by a readout (RO) pulse (red, not to scale). **b**, Rabi oscillation corresponding to $A = 0.1$ V, fit with $a\cos(t\Omega_R)\exp(t/t_d)$ (solid line). The fit yields a decay time $t_d = 27$ ns. The dark- and light-green lines indicate the FWHM of a π/2 and a π pulse, respectively. **c**, Extracted Rabi frequencies versus pulse amplitude, fit with a linear equation (solid line).

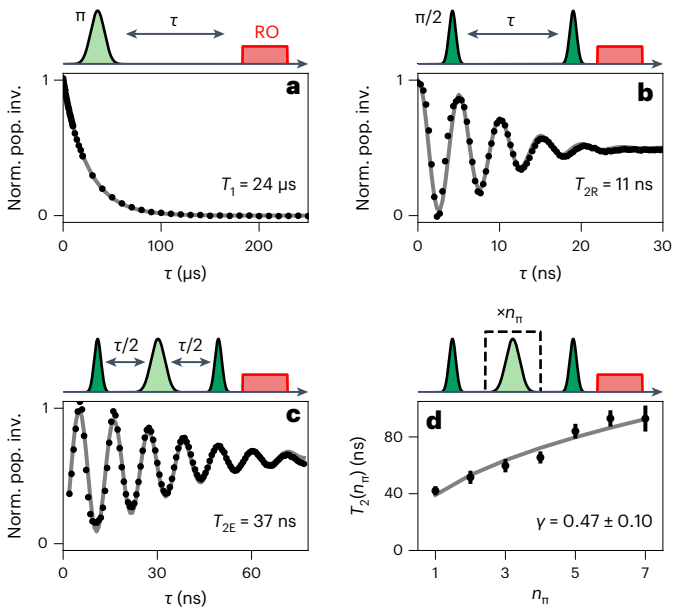

Fig. 3 | Coherence of the ASQ. Measured at the same setpoint as Fig. 2, for $A = 0.1$ V. **a**–**d**, Qubit lifetime (**a**), Ramsey (**b**), Hahn-echo (**c**) and Carr–Purcell (**d**) experiments. The solid lines indicate fits to the data. For **b**–**d**, oscillations are introduced into the decay by adding a phase proportional to the delay time for the final π/2 pulse. The data in **a**–**c** are obtained using a π pulse (π/2 pulse) with FWHM of 8 ns (4 ns), whereas for **d**, this value is 4 ns (2 ns). For **a**–**c**, we plot the normalized population inversion (norm. pop. inv.), where each sub-panel is individually normalized to the resulting fit. The markers and error bars in **d** represent the best-fit values and their estimated standard errors (1σ confidence intervals), respectively.

superconducting quantum interference device (SQUID) formed by the parallel combination of a gate-tunable Josephson junction with Josephson energy E_J, and the quantum dot Josephson junction hosting the ASQ. We operate in the regime $E_J/\sqrt{E_0^2 + E_{SO}^2} > 20$ so that the phase difference ϕ across the quantum dot Josephson junction can be controlled by the magnetic flux through the SQUID loop, namely, $\Phi_{ext} = \phi_{ext}\Phi_0/(2\pi)$, where $\Phi_0 = h/2e$ is the quantum of magnetic flux. Due to the presence of the E_{SO} term, the transmon frequency f_t becomes spin dependent. We exploit this fact to readout the ASQ state by capacitively coupling the transmon circuit to a readout resonator. Due to the transmon–resonator dispersive coupling, the resonator frequency, in turn, becomes spin dependent and probing the readout resonator, therefore, leads to a spin-dependent response. Spectroscopy of the spinful Andreev levels can, thus, be performed using standard two-tone circuit QED techniques[26]. Finally, the spin-flipping qubit transition can be directly driven and the transmon can be maintained in its ground state by applying a microwave tone on the central quantum dot gate[22,26,29]. Such a microwave drive allows for all-electrical manipulation through electric-dipole-induced spin resonance[23,24]. Supplementary Section II provides further details about the device implementation and setup.

Following the gate-tuning strategy described elsewhere[25], we prepare the quantum dot junction in a regime where it is occupied by an odd number of electrons, with $E_0/h = 211$ MHz and $E_{SO}/h = 305$ MHz and with a parity lifetime of 2.8 ms (Supplementary Section IIIC). In this regime, the qubit states $|\downarrow\rangle$ and $|\uparrow\rangle$ are the lowest-energy levels of the system, and the qubit subspace is separated from higher-lying states by a frequency gap of at least 20 GHz (Supplementary Section IIIA). After fixing the gate voltages of the quantum dot, we investigate the tunability of the spin-flip transition f_s by applying a microwave tone at frequency f_{drive} and performing dispersive readout of the transmon qubit. As shown in Fig. 1d, we can finely control f_s by applying a magnetic flux through the SQUID loop[30] (we attribute the shift in the minima and maxima of the spin-flip frequency away from π/2 and 3π/2 to the phase-dependent renormalization of the impurity g-factor by coupling to the leads, known as the impurity Knight shift), although the visibility of the measurement signal is reduced around $\phi_{ext} = 0$, π, where the spin-dependent transmon frequencies are degenerate[26]. By applying an external magnetic field along the nanowire B_z of up to 65 mT, the qubit frequency can be varied from 250 MHz to 12 GHz (Fig. 1e). The magnetic field direction is chosen to maximize the magnetic field compatibility of the Al shell of the nanowire and is generally not aligned with the spin–orbit direction $\vec{n}$ (refs. 26,31).

Qubit coherence

To perform the coherent manipulation of the spin states, we fix $B_z = 65$ mT and $\phi_{ext} = 3\pi/2$, setting $f_s = 11.5$ GHz, where the residual population of the excited state is suppressed to less than 5% (Supplementary Section IIID), facilitating qubit manipulation and readout. We observe Rabi oscillations between the qubit states $|\downarrow\rangle$ and $|\uparrow\rangle$ by applying a Gaussian microwave pulse with a carrier frequency at the spin-flip transition frequency $f_{drive} = f_s$ (Fig. 2). Here the Gaussian pulses are truncated so that the total pulse length is 2.5 times the Gaussian full-width at half-maximum (FWHM). As shown in Fig. 2a, we resolve up to ten oscillations by varying the amplitude and duration of the pulse envelope. The population transfer between the spin states, as measured by the dispersive readout scheme with a readout time of 2 μs, follows the expected time dependence of a standard Rabi oscillation (Fig. 2b), from which we extract the Rabi frequency for each pulse amplitude. For a fixed Rabi frequency, we calibrate the FWHM needed for π and π/2 pulses for single-qubit manipulation.

As expected for a two-level system, the Rabi frequency is linear over a wide range of pulse amplitudes. It only starts to deviate from this linear dependence for strong drive amplitudes (Fig. 2c). This deviation is due to the saturation of the maximum power provided by the room-temperature electronics[32]. We measure Rabi frequencies larger than 200 MHz, exceeding the largest Rabi frequencies achieved in SOQ[28] and more than an order of magnitude faster than previous

https://doi.org/10.1038/s41567-023-02071-x

results for the ASQ[19]. We observe that the Rabi frequency is approaching the anharmonicity of typical transmon qubits, with no indications of higher-order levels being driven. The two-level nature of the ASQ, thus, intrinsically supports faster single-qubit gates than standard transmon qubits[33].

Next, we characterize the lifetime of the ASQ by applying a π pulse and reading out the qubit state after a delay time τ. We obtain an exponential decay with a characteristic time $T_1 = 24.4 \pm 0.5$ μs at $B_z = 65$ mT (Fig. 3a). As a function of the magnetic field, T_1 varies between 10 and 40 μs for qubit frequencies above the transmon frequency. We conjecture that the observed lifetime is limited by Purcell-like decay from coupling to the transmon, given the short transmon lifetime of around 250 ns. For B_z closer to zero, T_1 drops down to around 1 μs (Supplementary Fig. 10). This low lifetime is in contrast to the near-zero-field lifetimes found in previous ASQ experiments[19,20], which were in the range of 10–50 μs. The cause of this discrepancy is unknown, but a potential reason is an enhanced resonant exchange with the nuclear spins[34] due to stronger strain in the InAs nanowire, which may vary for different nanowires depending on the exact growth conditions.

To characterize the coherence time of the qubit, we apply two π/2 pulses separated by a delay time, after which we read the qubit state. From this experiment, we extract a Ramsey coherence time of $T_{2R} = 11 \pm 1$ ns (Fig. 3b), much smaller than T_1, and thus indicative of strong dephasing. Dephasing that originates from slow noise compared with the spin dynamics can be partially cancelled using a Hahn-echo sequence[35], which introduces a π pulse halfway between the two π/2 pulses. This echo sequence increases the measured coherence time by more than three times, to $T_{2E} = 37 \pm 4$ ns (Fig. 3c).

The coherence time of the qubit can be further enhanced by using dynamical decoupling pulse sequences, which serve to filter out faster environmental fluctuations. We apply Carr–Purcell sequences[36–38], interleaving a varying number of equidistant π pulses, n_π, in between two π/2 pulses. As n_π increases, higher-frequency noise is cancelled out, extending the decoherence times. We reach T_2 times up to more than 90 ns for $n_\pi = 7$, at which stage we are most probably limited by decoherence during the π pulses (Fig. 3d and Supplementary Information). We subsequently fit the n_π dependence of T_2 with a power law, $T_2(n_\pi) \propto n_\pi^\gamma$. Assuming a noise power spectral density of the form $f^{A/\beta}$, we expect the relation $\beta = \gamma/(1-\gamma)$ (refs. 38–40). The observed scaling with $\gamma = 0.47 \pm 0.10$, therefore, suggests that the decoherence is governed by noise with a $1/f$ spectral density in the frequency range of 25–100 MHz.

There are several potential sources of dephasing that are compatible with a $1/f$ noise spectral density, such as flux noise through the SQUID loop and charge noise[41,42]. We exclude the former, as we do not observe an increase in coherence times at the flux sweet spots (Supplementary Fig. 12). Similarly, no consistent trend is observed when varying the gate voltages, nor when increasing the magnetic field strength. The latter indicates that charge noise is probably not the dominant contributor to dephasing, given that electric-dipole-induced spin resonance becomes more effective at coupling charge noise to the qubit at elevated fields[23,24,27,28]. Additionally, based on the evolution of the Rabi decay time with increasing pulse amplitudes[43], the size of the charge fluctuations required to cause the observed amount of dephasing is estimated to be 0.25 mV, substantially larger than what is expected to originate from the gate lines (Supplementary Section IIIH). However, the contribution of charge fluctuations originating elsewhere, such as in the dielectric material on the device, could still be contributing to the dephasing. Given that the sensitivity to fluctuations in environmental offset charge on the transmon island is suppressed by the large $E_J/E_c > 30$ ratio, it is furthermore improbable that the ASQ dephasing originates from offset-charge-dependent fluctuations of the transmon frequency qubit[3].

Another potential source of dephasing originates from the dynamics of the spinful nuclei in the nanowire, which may couple to the ASQ as a result of the hyperfine interaction. It has previously been shown that these dynamics can lead to longitudinal Overhauser field fluctuations with a $1/f$ spectral density[44]. Moreover, this effect is expected to be particularly strong in InAs due to the large nuclear spin of indium ($I = 9/2$) and should not be strongly affected by the magnetic field in the B_z range investigated here, which is not enough to polarize the nuclear spins. Corroborated by the fact that the extracted T_{2R} and T_{2E} times are strikingly similar to those found for the weak-link InAs ASQ[19], InAs SOQ[24] and InSb SOQ[28], we conjecture that the nuclear environment provides a notable contribution to the decoherence of the ASQ.

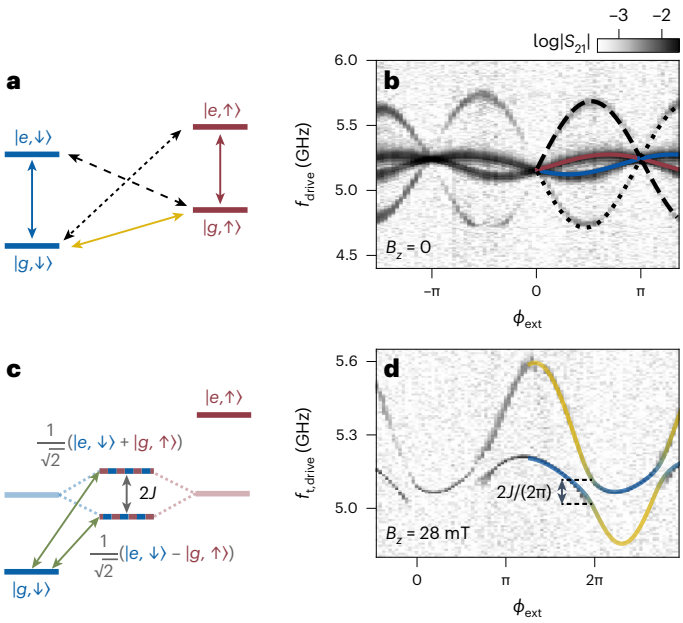

Fig. 4 | Coherent ASQ–transmon coupling. a, Frequency diagram of the joint ASQ–transmon circuit (Fig. 1c) at large detuning between the ASQ and transmon qubit energy levels. In addition to the two spin-conserving transmon transitions (solid red and blue) and the transmon-conserving spin qubit transition (solid yellow), two additional transitions involving both qubits can take place in the presence of coherent coupling between them (dashed and dotted black). **b**, Two-tone spectroscopy of the joint two-qubit system at $B_z = 0$. In addition to the two spin-dependent branches of the transmon qubit frequency[26], two additional transitions appear. The transition frequencies obtained from the model of equation (2) are overlaid. **c**, Frequency diagram of the joint ASQ–transmon circuit for $|e,\downarrow\rangle = |g,\uparrow\rangle$. In the presence of coherent coupling, the two qubits hybridize into states with a frequency splitting of $2J$. The green arrows denote the transitions from ground to the two hybridized states. **d**, Two-tone spectroscopy versus external flux at $B_z = 28$ mT, where $f_s \approx f_t$. This results in avoided crossings between the two qubit frequencies. The transition frequencies obtained from the model of equation (2) are overlaid. Their colours denote the expectation value of the spin degree of freedom of the excited state and go from $|\downarrow\rangle$ (blue) for the transmon transition to $|\uparrow\rangle$ (yellow) for the spin-flip transition. Here $f_{t,drive}$ denotes the frequency of the second tone, sent through the readout resonator.

ASQ–transmon coupling

One of the main characteristics of the ASQ is the intrinsic coupling between the spin degree of freedom and the supercurrent across the quantum dot Josephson junction. We have, so far, only exploited this coupling for readout of the qubit state using circuit QED techniques. Now, we demonstrate the observation of coherent coupling of the ASQ with the transmon qubit.

The first signature of a coherent coupling is the presence of transitions that involve both qubits, in addition to the single-qubit transitions (Fig. 4a). At zero applied magnetic field, we spectroscopically detect two of such transitions at $f_t + f_s$ and $f_t - f_s$, where f_t is the transmon

frequency (Fig. 4b). We classify them based on a fit with the joint Hamiltonian of the total ASQ–transmon circuit (Fig. 1c) given by

$$H_{\mathrm{tot}} = -4E_{\mathrm{c}}\partial_{\phi}^{2} - E_{\mathrm{J}}\cos(\phi - \phi_{\mathrm{ext}}) + H_{\mathrm{s}}(\phi). \quad (2)$$

We identify the additional observed resonances as the double excitation $|g,\downarrow\rangle \leftrightarrow |e,\uparrow\rangle$ and the $|g,\uparrow\rangle \leftrightarrow |e,\downarrow\rangle$ SWAP transitions, where $|g\rangle$ and $|e\rangle$ denote the ground and first excited transmon states, respectively. These transitions could be used to construct entanglement and two qubit gates between the two different qubit platforms, provided the transitions can be driven at a faster rate than the decoherence rates of either qubit.

Additionally, one of the hallmarks of strong coherent coupling is the appearance of an avoided-level crossing when both qubit frequencies are made equal, that is, $f_{\mathrm{t}} \approx f_{\mathrm{s}}$. In this case, the $|e,\downarrow\rangle$ and $|g,\uparrow\rangle$ states are expected to hybridize into superposition states with a frequency splitting of $2J$ (Fig. 4c). At $B_z = 28$ mT, this splitting can be readily observed in the experiment. By varying the external flux ϕ_{ext} such that the ASQ frequency f_{s} crosses the transmon frequency f_{t}, we find avoided crossings with a minimum frequency splitting of $2J/(2\pi) = 2 \times 52$ MHz (Fig. 4d). As J is four times larger than the decoherence rate of the ASQ, $1/T_{2\mathrm{R}} \approx 14.0 \times 2\pi$ MHz and one order of magnitude larger than the decoherence rate of the transmon ($\sim 1.2 \times 2\pi$ MHz), the coupling between the two qubits falls into the strong-coupling regime. This result establishes the first realization of a direct strong coupling between a spin qubit and a superconducting qubit, in contrast to the results of another work[45] in which a high-impedance bus resonator was required to mediate the coupling between the spin and transmon qubit through virtual photons.

Analytical estimates predict that the coupling $J \propto E_{\mathrm{SO}}\phi_{\mathrm{zpf}}\sin(\theta)$, where ϕ_{zpf} is the magnitude of the zero-point fluctuation of the transmon phase and θ is the angle between the Zeeman field and the spin–orbit direction $\vec{n}$ (Supplementary Section IB). This expression suggests that by choosing a resonance with a larger E_{SO} (ref. 26) and by aligning the magnetic field perpendicular to the spin–orbit direction, coupling rates of hundreds of megahertz can be achieved, which would enable rapid two-qubit gates between the transmon and ASQ and potentially allow for the study of light–matter interactions in the ultrastrong-coupling regime[46,47].

Towards new platforms and multiple ASQs

We have implemented an ASQ, where the spin degree of freedom of a quasiparticle in a quantum dot with superconducting leads encodes the qubit state. The qubit subspace is stabilized by the charging energy of the quantum dot and direct microwave driving of the transitions is possible without the requirement of auxiliary levels. The qubit coherence was found to be comparable with previous results for qubits implemented in InAs or InSb nanowires[19,24,28]. Our results suggest that the nuclear environment strongly contributes to the ASQ decoherence, although the contribution of charge noise cannot be fully neglected. This limitation motivates future investigations of alternative material platforms for ASQs, such as superconductor-proximitized nuclear-spin-free semiconductors[48], for example, isotopically purified germanium[49–51].

We furthermore observed direct strong coherent coupling between the ASQ and transmon qubit. Such strong coupling showcases the advantage of the intrinsic spin–supercurrent coupling, allowing the ASQ to be readily integrated into a circuit QED architecture. Our results open avenues towards multiqubit devices: we propose to leverage the fact that transmon qubits can be readily coupled together using capacitive coupling, useful for mediating interactions between multiple ASQs. Furthermore, our results are a crucial step towards the coupling of distant ASQs through bus resonators or a shared inductance[17], as well as short-distance coupling through wavefunction overlap[52].

Online content

Any methods, additional references, Nature Portfolio reporting summaries, source data, extended data, supplementary information, acknowledgements, peer review information; details of author contributions and competing interests; and statements of data and code availability are available at https://doi.org/10.1038/s41567-023-02071-x.

References

1. Loss, D. & DiVincenzo, D. P. Quantum computation with quantum dots. *Phys. Rev. A* **57**, 120 (1998).
2. Hanson, R., Kouwenhoven, L. P., Petta, J. R., Tarucha, S. & Vandersypen, L. M. K. Spins in few-electron quantum dots. *Rev. Mod. Phys.* **79**, 1217 (2007).
3. Koch, J. et al. Charge-insensitive qubit design derived from the Cooper pair box. *Phys. Rev. A* **76**, 042319 (2007).
4. Zwerver, A. M. J. et al. Qubits made by advanced semiconductor manufacturing. *Nat. Electron.* **5**, 184–190 (2022).
5. Mi, X. et al. A coherent spin–photon interface in silicon. *Nature* **555**, 599–603 (2018).
6. Samkharadze, N. et al. Strong spin-photon coupling in silicon. *Science* **359**, 1123–1127 (2018).
7. Landig, A. J. et al. Coherent spin–photon coupling using a resonant exchange qubit. *Nature* **560**, 179–184 (2018).
8. Borjans, F., Croot, X. G., Mi, X., Gullans, M. J. & Petta, J. R. Resonant microwave-mediated interactions between distant electron spins. *Nature* **577**, 195–198 (2020).
9. Harvey-Collard, P. et al. Coherent spin-spin coupling mediated by virtual microwave photons. *Phys. Rev. X* **12**, 021026 (2022).
10. Yu, C. X. et al. Strong coupling between a photon and a hole spin in silicon. *Nat. Nanotechnol.* https://doi.org/10.1038/s41565-023-01332-3 (2023).
11. Arute, F. et al. Quantum supremacy using a programmable superconducting processor. *Nature* **574**, 505–510 (2019).
12. *Compute Resources* (IBM Quantum, accessed 13 June 2022); https://quantum-computing.ibm.com/services?services=systems
13. Blais, A. et al. Cavity quantum electrodynamics for superconducting electrical circuits: an architecture for quantum computation. *Phys. Rev. A* **69**, 062320 (2004).
14. Wallraff, A. et al. Strong coupling of a single photon to a superconducting qubit using circuit quantum electrodynamics. *Nature* **431**, 162–167 (2004).
15. Blais, A., Grimsmo, A. L., Girvin, S. & Wallraff, A. Circuit quantum electrodynamics. *Rev. Mod. Phys.* **93**, 025005 (2021).
16. Chtchelkatchev, N. M. & Nazarov, Y. V. Andreev quantum dots for spin manipulation. *Phys. Rev. Lett.* **90**, 226806 (2003).
17. Padurariu, C. & Nazarov, Y. V. Theoretical proposal for superconducting spin qubits. *Phys. Rev. B* **81**, 144519 (2010).
18. Béri, B., Bardarson, J. H. & Beenakker, C. W. J. Splitting of Andreev levels in a Josephson junction by spin-orbit coupling. *Phys. Rev. B* **77**, 045311 (2008).
19. Hays, M. et al. Coherent manipulation of an Andreev spin qubit. *Science* **373**, 430–433 (2021).
20. Hays, M. et al. Continuous monitoring of a trapped superconducting spin. *Nat. Phys.* **16**, 1103–1107 (2020).
21. Park, S. & Yeyati, A. L. Andreev spin qubits in multichannel Rashba nanowires. *Phys. Rev. B* **96**, 125416 (2017).
22. Metzger, C. et al. Circuit-QED with phase-biased Josephson weak links. *Phys. Rev. Research* **3**, 013036 (2021).
23. Nowack, K. C., Koppens, F. H. L., Nazarov, Y. V. & Vandersypen, L. M. K. Coherent control of a single electron spin with electric fields. *Science* **318**, 1430–1433 (2007).
24. Nadj-Perge, S., Frolov, S. M., Bakkers, E. P. A. M. & Kouwenhoven, L. P. Spin–orbit qubit in a semiconductor nanowire. *Nature* **468**, 1084–1087 (2010).

25. Bargerbos, A. et al. Singlet-doublet transitions of a quantum dot Josephson junction detected in a transmon circuit. *PRX Quantum* **3**, 030311 (2022).
26. Bargerbos, A. et al. Spectroscopy of spin-split Andreev levels in a quantum dot with superconducting leads. Preprint at https://arxiv.org/abs/2208.09314 (2022).
27. Golovach, V. N., Borhani, M. & Loss, D. Electric-dipole-induced spin resonance in quantum dots. *Phys. Rev. B* **74**, 165319 (2006).
28. van den Berg, J. W. G. et al. Fast spin-orbit qubit in an indium antimonide nanowire. *Phys. Rev. Lett.* **110**, 066806 (2013).
29. Wesdorp, J. J. et al. Microwave spectroscopy of interacting Andreev spins. Preprint at https://arxiv.org/abs/2208.11198 (2022).
30. Pavešić, L., Pita-Vidal, M., Bargerbos, A. & Žitko, R. Impurity Knight shift in quantum dot Josephson junctions. Preprint at https://arxiv.org/abs/2212.07185 (2022).
31. Han, L. et al. Variable and orbital-dependent spin-orbit field orientations in an InSb double quantum dot characterized via dispersive gate sensing. *Phys. Rev. Appl.* **19**, 014063 (2023).
32. Lazăr, S. et al. Calibration of drive non-linearity for arbitrary-angle single-qubit gates using error amplification. Preprint at https://arxiv.org/abs/2212.01077 (2022).
33. Werninghaus, M. et al. Leakage reduction in fast superconducting qubit gates via optimal control. *npj Quantum Inf.* **7**, 14 (2021).
34. Stockill, R. et al. Quantum dot spin coherence governed by a strained nuclear environment. *Nat. Commun.* **7**, 12745 (2016).
35. Hahn, E. L. Spin echoes. *Phys. Rev.* **80**, 580 (1950).
36. Carr, H. Y. & Purcell, E. M. Effects of diffusion on free precession in nuclear magnetic resonance experiments. *Phys. Rev.* **94**, 630 (1954).
37. Barthel, C., Medford, J., Marcus, C. M., Hanson, M. P. & Gossard, A. C. Interlaced dynamical decoupling and coherent operation of a singlet-triplet qubit. *Phys. Rev. Lett.* **105**, 266808 (2010).
38. Bylander, J. et al. Noise spectroscopy through dynamical decoupling with a superconducting flux qubit. *Nat. Phys.* **7**, 565–570 (2011).
39. Cywiński, L., Lutchyn, R. M., Nave, C. P. & Das Sarma, S. How to enhance dephasing time in superconducting qubits. *Phys. Rev. B* **77**, 174509 (2008).
40. Medford, J. et al. Scaling of dynamical decoupling for spin qubits. *Phys. Rev. Lett.* **108**, 086802 (2012).
41. Schreier, J. A. et al. Suppressing charge noise decoherence in superconducting charge qubits. *Phys. Rev. B* **77**, 180502 (2008).
42. Braumüller, J. et al. Characterizing and optimizing qubit coherence based on SQUID geometry. *Phys. Rev. Appl.* **13**, 054079 (2020).
43. Malinowski, F. K. et al. Symmetric operation of the resonant exchange qubit. *Phys. Rev. B* **96**, 045443 (2017).
44. Malinowski, F. K. et al. Spectrum of the nuclear environment for GaAs spin qubits. *Phys. Rev. Lett.* **118**, 177702 (2017).
45. Landig, A. J. et al. Virtual-photon-mediated spin-qubit–transmon coupling. *Nat. Commun.* **10**, 5037 (2019).
46. Forn-Díaz, P., Lamata, L., Rico, E., Kono, J. & Solano, E. Ultrastrong coupling regimes of light-matter interaction. *Rev. Mod. Phys.* **91**, 025005 (2019).
47. Scarlino, P. et al. In situ tuning of the electric-dipole strength of a double-dot charge qubit: charge-noise protection and ultrastrong coupling. *Phys. Rev. X* **12**, 031004 (2022).
48. de Leon, N. P. et al. Materials challenges and opportunities for quantum computing hardware. *Science* **372**, eabb2823 (2021).
49. Hendrickx, N. W. et al. Gate-controlled quantum dots and superconductivity in planar germanium. *Nat. Commun.* **9**, 2835 (2018).
50. Scappucci, G. et al. The germanium quantum information route. *Nat. Rev. Mater.* **6**, 926–943 (2021).
51. Tosato, A. et al. Hard superconducting gap in germanium. *Commun. Mater.* **4**, 23 (2023).
52. Spethmann, M., Zhang, X.-P., Klinovaja, J. & Loss, D. Coupled superconducting spin qubits with spin-orbit interaction. *Phys. Rev. B* **106**, 115411 (2022).

Data availability

The data that support the findings of this study are publicly available via 4TU.ResearchData at https://doi.org/10.4121/c.6073271.

Code availability

The analysis code that supports the findings of this study is publicly available via 4TU.ResearchData at https://doi.org/10.4121/c.6073271.

Acknowledgements

We acknowledge fruitful discussion with M. Veldhorst, M. Russ, F. Malinowski, V. Fatemi and Y. Nazarov. We further thank P. Krogstrup for guidance in the material growth. This research was inspired by prior work by J.J.W. where the spin-flip transition in an InAs/Al nanowire weak link was directly observed in spectroscopy under the application of a magnetic field[29]. This research is co-funded by the allowance for Top Consortia for Knowledge and Innovation (TKI) from the Dutch Ministry of Economic Affairs; research project 'Scalable circuits of Majorana qubits with topological protection' (i39, SCMQ) with project no. 14SCMQ02; the Dutch Research Council (NWO); and the Microsoft Quantum initiative. R.Ž. acknowledges support from the Slovenian Research Agency (ARRS) under P1-0416 and J1-3008. R.A. acknowledges support from the Spanish Ministry of Science and Innovation through grant PGC2018-097018-B-I00 and from the CSIC Research Platform on Quantum Technologies PTI-001. B.v.H. and C.K.A. acknowledge support from the Dutch Research Council (NWO).

Author contributions

A.B., M.P.-V. and A.K. conceived the experiment. Y.L. developed and provided the nanowire materials. A.B., M.P.-V., L.J.S., L.G. and J.J.W. prepared the experimental setup and data acquisition tools. L.J.S. deposited the nanowires. A.B. and M.P.-V. designed and fabricated the device, performed the measurements and analysed the data, with continuous feedback from L.J.S., L.G., J.J.W., B.v.H., A.K. and C.K.A. R.A., B.v.H. and R.Ž. provided theory support during and after the measurements. A.B., M.P.-V. and B.v.H. wrote the code to compute the circuit energy levels and extract the experimental parameters. L.P.K., R.A., B.v.H., A.K. and C.K.A. supervised the work. A.B., M.P.-V. and C.K.A. wrote the paper with feedback from all authors.

Competing interests

The authors declare no competing interests.

Additional information

Supplementary information The online version contains supplementary material available at https://doi.org/10.1038/s41567-023-02071-x.

Correspondence and requests for materials should be addressed to Marta Pita-Vidal or Christian Kraglund Andersen.

Peer review information *Nature Physics* thanks the anonymous reviewers for their contribution to the peer review of this work.